Inertial migration in dilute and semidilute suspensions of rigid particles in laminar square duct flow

H. Tabaei Kazerooni[*]
SeRC and Linné FLOW Centre, KTH Mechanics, 10044 Stockholm, Sweden and Chair of Hydraulic Fluid Machinery, Ruhr-Universität Bochum, Universitätsstraße 150, 44801 Bochum, Germany

W. Fornari[†]
SeRC and Linné FLOW Centre, KTH Mechanics, 10044 Stockholm, Sweden

J. Hussong[‡]
Chair of Hydraulic Fluid Machinery, Ruhr-Universität Bochum, Universitätsstraße 150, 44801 Bochum, Germany

L. Brandt[§]
SeRC and Linné FLOW Centre, KTH Mechanics, 10044 Stockholm, Sweden
(Received 29 December 2016; published 8 August 2017)

We study the inertial migration of finite-size neutrally buoyant spherical particles in dilute and semidilute suspensions in laminar square duct flow. We perform several direct numerical simulations using an immersed boundary method to investigate the effects of the bulk Reynolds number Re_b, particle Reynolds number Re_p, and duct to particle size ratio h/a at different solid volume fractions ϕ, from very dilute conditions to 20%. We show that the bulk Reynolds number Re_b is the key parameter in inertial migration of particles in dilute suspensions. At low solid volume fraction ($\phi = 0.4\%$), low bulk Reynolds number ($\mathrm{Re}_b = 144$), and $h/a = 9$ particles accumulate at the center of the duct walls. As Re_b is increased, the focusing position moves progressively toward the corners of the duct. At higher volume fractions, $\phi = 5\%$, 10%, and 20%, and in wider ducts ($h/a = 18$) with $\mathrm{Re}_b = 550$, particles are found to migrate away from the duct core toward the walls. In particular, for $\phi = 5\%$ and 10%, particles accumulate preferentially at the corners. At the highest volume fraction considered, $\phi = 20\%$, particles sample all the volume of the duct, with a lower concentration at the duct core. For all cases, we find that particles reside longer times at the corners than at the wall centers. In a duct with lower duct to particle size ratio $h/a = 9$ (i.e., with larger particles), $\phi = 5\%$, and high bulk Reynolds number $\mathrm{Re}_b = 550$, we find a particle concentration pattern similar to that in the ducts with $h/a = 9$ regardless of the solid volume fraction ϕ. Instead, for lower Bulk Reynolds number $\mathrm{Re}_b = 144$, $h/a = 9$, and $\phi = 5\%$, a different particle distribution is observed in comparison to a dilute suspension $\phi = 0.4\%$. Hence, the volume fraction plays a key role in defining the final distribution of particles in semidilute suspensions at low bulk Reynolds number. The presence of particles induces secondary cross-stream motions in the duct cross section, for all ϕ. The intensity of these secondary flows depends strongly on particle rotation rate, on the maximum concentration of particles in focusing positions, and on the solid volume fraction. We find that the secondary flow intensity increases with the volume fraction up to $\phi = 5\%$. However, beyond $\phi = 5\%$ excluded-volume effects lead to a strong reduction of cross-stream velocities for $\mathrm{Re}_b = 550$ and $h/a = 18$. Inhibiting particles from rotating

[*]seyed.tabaeikazerooni@rub.de
[†]fornari@mech.kth.se
[‡]jeanette.hussong@rub.de
[§]luca@mech.kth.se

also results in a substantial reduction of the secondary flow intensity and in variations of the exact location of the focusing positions.

DOI: 10.1103/PhysRevFluids.2.084301

I. INTRODUCTION

The role and the importance of fluid inertia in different microfluidic applications has recently been recognized [1]. Due to finite fluid inertia, for example, it is possible to achieve enhanced mixing and efficient particle separation and focusing. To further develop inertial microfluidic devices, it is therefore necessary to properly understand the behavior of suspensions at finite Reynolds numbers and in confined geometries.

Clearly, these suspensions exhibit very interesting and peculiar rheological properties. Among these we recall shear thinning or thickening, the appearance of normal stress differences, and jamming at high volume fractions [2,3]. Interesting effects due to confinement in simple shear flows in the Stokes and weakly inertial regimes have also been reported recently [4,5]. Another important feature observed in wall-bounded flows is particle migration. In the viscous regime, there is an irreversible shear-induced migration of particles away from channel walls [6]. However, when inertial effects become important the migration mechanisms may vary. This is typically referred to simply as inertial migration.

The inertial migration of neutrally buoyant finite-size particles in Poiseuille flow has been the object of several studies since the work by Segre and Silberberg [7]. These authors studied experimentally the flow of a dilute suspension of randomly distributed spherical particles in a laminar pipe flow. They showed that, at very low bulk Reynolds number $\mathrm{Re}_b = O(1)$, particles migrate away from the pipe core region and form a stable annulus at a distance of approximately $0.6R$, with R the pipe radius. It was later explained that the particle equilibrium position in the pipe cross section is determined by the balance between the wall repulsive lubrication force [8] and the shear-induced lift force on the particle due to the curvature of the velocity profile [9]. Matas *et al.* [10] studied experimentally the effects of the bulk Reynolds number Re_b and pipe to particle size ratio on the inertial migration of spherical particles at low volume fractions $\phi < 1\%$. These experiments show that particles are progressively pushed toward the wall as the bulk Reynolds number is increased. However, at larger Re_b and depending on the pipe to particle size ratio, it was also found that particles accumulate on an inner annulus in the pipe cross section. Later on, the same authors [11] performed an asymptotic analysis to investigate the equilibrium position of a sphere in laminar pipe flow based on the point particle assumption. While this theoretical work confirmed the progressive shift of the particle toward the pipe wall by increasing the bulk Reynolds number Re_b, it could not predict the presence of the inner particle annulus closer to the pipe center. Hence, the existence of the inner equilibrium position is probably related to the finite size of the particles. Most recently, Morita *et al.* [12] performed several experiments to clarify this discrepancy between theoretical and experimental results and suggested that the occurrence of the inner annulus is a transient phenomenon that would disappear for long enough pipes for $\mathrm{Re}_b < 1000$ and tube to particle diameter ratios of $\sim$12. Concerning dense suspensions of neutrally buoyant particles in pipe flows, Han *et al.* [13] showed experimentally that inertial migration is a very robust phenomenon that occurs for particle Reynolds numbers Re_p larger than 0.1 even at moderately high solid volume fraction $\phi \sim 30\%$.

In the past few years, the Segre-Silberberg phenomenon has been used as a passive method for the separation and sorting of cells and particles in microfluidic devices [1,14,15]. Details on the physics of inertial migration and its microfluidic applications have been documented recently in a comprehensive review article by Amini *et al.* [16]. Due to microchip manufacturing, square channels are often utilized in such applications. Due to the loss of cylindrical symmetry, the particle behavior is altered with respect to pipe flows. The study of particulate duct flows has hence attracted various researchers over the years.

Chun and Ladd [17], for example, performed numerical simulations using a lattice-Boltzmann method to study the motion of single particles and dilute suspensions in square duct flows. The existence of eight equilibrium positions at the duct corners and wall centers was reported for single particles in a range of bulk Reynolds number Re_b between 100 and 1000. It was shown that at moderately high Reynolds numbers ($\mathrm{Re}_b > 500$), the equilibrium position at the wall center is not stable and particles move toward the duct corners. A similar pattern was found for a low solid volume fraction ($\phi = 1\%$) at $\mathrm{Re}_b = 500$. Moreover, the appearance of particles at the inner region of the duct was also observed in addition to four equilibrium positions at the corners for $\phi = 1\%$ and $\mathrm{Re}_b = 1000$. However, as previously discussed, it seems that the presence of the particles in the center region of Poiseuille flows of dilute suspensions at high bulk Reynolds number Re_b is a transient feature.

Later, Di Carlo *et al.* [18] carried out an experimental and numerical investigation of the motion of an individual particle in duct flow at low Reynolds number. In particular, they explored the lift forces acting on the particle and the influence of the particle to duct size ratio on the particle equilibrium position. They showed that for low bulk Reynolds number the duct corners are unstable equilibrium positions. The duct wall centers are the only points where the wall lubrication and shear-induced lift forces balance each other and are hence stable equilibrium positions. These results have also been confirmed recently by the theoretical work of Hood *et al.* [19] in which an asymptotic model was used to predict the lateral forces on a particle and determine its stable equilibrium position.

Choi *et al.* [20] investigated experimentally the spatial distribution of dilute suspended particles in a duct flow at low bulk Reynolds numbers ($\mathrm{Re}_b < 120$) and different duct to particle size ratios h/a (where h and a are the duct half-width and the particle radius, respectively). For $\mathrm{Re}_b = 12$ and relatively high duct to particle size ratio ($h/a = 6.25$), they observed the formation of a ring of particles parallel to the duct walls at a distance of around $0.6h$ from the centerline. They showed that by increasing the bulk Reynolds number to 120, the particle ring breaks and four particle focusing (equilibrium) points are observed at the duct wall centers. The same behavior for particle distributions across the duct cross section has also been observed experimentally by Abbas *et al.* [21] for $\mathrm{Re}_b \in [0.07; 120]$. On the other hand, for very low Reynolds number $\mathrm{Re} \ll 1$ (i.e., when inertia is negligible), particles accumulate at the duct center region. More recently, Miura *et al.* [22] carried out an experimental study on the inertial migration of particles in a macroscale square duct for $h/a = 9.2$ and for $\mathrm{Re}_b \in [100; 1200]$. They showed that the corner equilibrium position appears only at relatively high Reynolds number ($\mathrm{Re}_b > 250$). These results were later confirmed by Nakagawa *et al.* [23], who studied numerically the migration of a rigid sphere in duct flow, in a range of bulk Reynolds number Re_b from 20 to 1000. In particular, these authors showed that the equilibrium position at the duct corner is unstable until the bulk Reynolds number Re_b exceeds a critical value ($\mathrm{Re}_b \approx 260$). At this Re_b, additional equilibrium positions are shown to appear on the heteroclinic orbits close to the corners. Finally, in a recent paper Lashgari *et al.* [24] performed numerical simulations to study the inertial migration of oblate particles in squared and rectangular ducts.

Despite a considerable number of studies on particulate duct flows, the physical understanding of the effects observed is not complete and the range of parameters still unexplored is vast. For example, as said before, most experimental and numerical studies focused on dilute suspensions of particles, while the flow at higher solid volume fractions has not yet been investigated thoroughly, a relevant aspect for high-throughput applications. Therefore, the main goal of the present study is to fill this gap by exploring particle and flow behavior in a square duct at relatively high particle concentrations covering the range of solid volume fraction $\phi = 0.4\%$–20%. To this end, we perform interface-resolved numerical simulations using an immersed boundary method with lubrication and collision models for short-range interactions. We report the spatial distribution of particles across the duct cross section for $\phi = 0.4\%$–20% at constant bulk Reynolds number $\mathrm{Re}_b = 550$ and $h/a = 18$. Overall, we observe that particles depart from the duct core region and accumulate around the duct walls and preferentially in the duct corners. The same particle concentration pattern is observed for $\phi = 5\%$ at bulk Reynolds number $\mathrm{Re}_b = 550$ and $h/a = 9$, i.e., larger particles. In addition, we show

that for high solid volume fraction $\phi = 20\%$ at low bulk Reynolds number $\mathrm{Re}_b = 144$ and $h/a = 9$, particle concentrate at the duct center region and inertial migration of particles is almost lost. We also investigate the effects of the bulk and particle Reynolds numbers and the duct to particle size ratio on the behavior of a dilute suspension with $\phi = 0.4\%$. The particular focusing positions depend mostly on the bulk Reynolds number Re_b. Changing the duct to particle size ratio h/a, particle inertia varies independently of fluid inertia in each case and this leads to different specific arrangements of particles around the equilibrium positions. Finally, we show that the presence of particles alters the flow in such a way that cross-stream secondary vortices appear around the particle focusing positions at low solid volume fraction $\phi = 0.4\%$. The intensity of these secondary flows depends on the maximum concentration of particles at these locations. For semidilute suspensions ($\phi \geqslant 5\%$) at bulk Reynolds number $\mathrm{Re}_b = 550$ and $h/a = 18$, the presence of particles induces a pair of cross-stream secondary vortices at the duct corners. At high solid volume fraction ($\phi = 20\%$), the duct core region is never fully depleted of particles and the intensity of secondary flows is substantially reduced. Overall, the mean secondary flow intensity initially increases with ϕ and then decreases for $\phi > 5\%$. We will also show that particle rotation plays an important role in determining the focusing positions as well as the intensity of the secondary flows.

II. METHODOLOGY

A. Numerical method

In this study the immersed boundary method (IBM) proposed by Breugem [25] is used to simulate dilute and semidilute suspensions of neutrally buoyant spherical particles in square ducts. The flow field is described on a Eulerian grid by the incompressible Navier-Stokes equations

$$\nabla \cdot \mathbf{u}_f = 0, \tag{1}$$

$$\frac{\partial \mathbf{u}_f}{\partial t} + \mathbf{u}_f \cdot \nabla \mathbf{u}_f = -\frac{1}{\rho_f} \nabla p + \nu \nabla^2 \mathbf{u}_f + \mathbf{f}, \tag{2}$$

where p and $\mathbf{u}_f$ are the pressure and velocity fields and ν and ρ_f are the kinematic viscosity and density of the fluid phase. The last term on the right-hand side of Eq. (2), $\mathbf{f}$, is the IBM force field imposed on the flow to model the boundary condition at the moving particle surface (i.e., $\mathbf{u}_f|_{\partial \mathcal{V}_p} = \mathbf{u}_p + \boldsymbol{\omega}_p \times \mathbf{r}$). The dynamics of the rigid particles is governed by the Newton-Euler Lagrangian equations

$$\rho_p V_p \frac{d\mathbf{u}_p}{dt} = \oint_{\partial \mathcal{V}_p} \boldsymbol{\tau} \cdot \mathbf{n} \, dS, \tag{3}$$

$$I_p \frac{d\boldsymbol{\omega}_p}{dt} = \oint_{\partial \mathcal{V}_p} \mathbf{r} \times \boldsymbol{\tau} \cdot \mathbf{n} \, dS, \tag{4}$$

where $\mathbf{u}_p$ and $\boldsymbol{\omega}_p$ are the linear and angular velocities of the particle centroid. In Eqs. (3) and (4), $V_p = 4\pi a^3/3$ and $I_p = 2\rho_p V_p a^2/5$ represent the particle volume and moment of inertia, $\boldsymbol{\tau} = -p\mathbf{I} + 2\nu\rho_f(\nabla \mathbf{u}_f + \nabla \mathbf{u}_f^T)/2$ is the fluid stress tensor, and $\mathbf{r}$ indicates the distance from the center of the particles ($\mathbf{n}$ is the unity vector normal to the particle surface $\partial \mathcal{V}_p$).

The fluid phase is evolved entirely on a uniform staggered Cartesian grid using a second-order finite-difference scheme. An explicit third-order Runge-Kutta scheme has been combined with a pressure-correction method to perform the time integration at each substep. This latter integration scheme has also been used for the evolution of Eqs. (3) and (4). Each particle surface is described by N_L uniformly distributed Lagrangian points. The force exchanged by the fluid on the particles is imposed on each lth Lagrangian point. This force is related to the Eulerian force field $\mathbf{f}$ by the expression $\mathbf{f}(\mathbf{x}) = \sum_{l=1}^{N_L} \hat{\mathbf{F}}_l \delta_d(\mathbf{x} - \mathbf{X}_l)\Delta V_l$, where ΔV_l is the volume of the cell containing the lth Lagrangian point and δ_d is the Dirac delta. Here $\hat{\mathbf{F}}_l$ is the force (per unit mass) at each Lagrangian

point and it is computed as $\hat{\mathbf{F}}_l = [\mathbf{U}_p(\mathbf{X}_l) - \mathbf{U}_l^*]/\Delta t$, where $\mathbf{U}_p = \mathbf{u}_p + \boldsymbol{\omega}_p \times \mathbf{r}$ is the velocity at the Lagrangian point l at the previous time step and $\mathbf{U}_l^*$ is the interpolated first prediction velocity at the same point.

An iterative algorithm with second-order global accuracy in space is employed to calculate this force field. To maintain accuracy, Eqs. (3) and (4) are rearranged in terms of the IBM force field,

$$\rho_p V_p \frac{d\mathbf{u}_p}{dt} = -\rho_f \sum_{l=1}^{N_l} \hat{\mathbf{F}}_l \Delta V_l + \rho_f \frac{d}{dt} \int_{\mathcal{V}_p} \mathbf{u}_f dV, \tag{5}$$

$$I_p \frac{d\boldsymbol{\omega}_p}{dt} = -\rho_f \sum_{l=1}^{N_l} \mathbf{r}_l \times \hat{\mathbf{F}}_l \Delta V_l + \rho_f \frac{d}{dt} \int_{\mathcal{V}_p} \mathbf{r} \times \mathbf{u}_f dV, \tag{6}$$

where $\mathbf{r}_l$ is the distance between the center of a particle and the lth Lagrangian point on its surface. The second terms on the right-hand sides are corrections that account for the inertia of the fictitious fluid contained within the particle volume. Particle-particle and particle-wall interactions are also considered. Well-known models based on Brenner's asymptotic solution [26] are employed to correctly predict the lubrication force when the gap distance between particles and between particles and walls is smaller than twice the mesh size. A soft-sphere collision model is used to account for particle-particle and particle-wall collisions. An almost elastic rebound is ensured with a restitution coefficient set at 0.97. Friction among particles and among particles and walls is also considered [27]. These lubrication and collision forces are added to the right-hand side of Eq. (5). A more detailed discussion of the numerical method and of the mentioned models can be found in previous publications [25,28–31]. Periodic boundary conditions are imposed in the streamwise direction. In the remaining directions, the stress immersed boundary method is used to impose the no-slip and no-penetration conditions at the walls. The stress immersed boundary method was originally developed to simulate the flow around rectangular-shaped obstacles in a fully Cartesian grid [32]. In this work we use this method to enforce the fluid velocity to be zero at the duct walls. For more details on the method, the reader is referred to the works of Breugem and Boersma [33] and Pourquie *et al.* [34].

B. Flow configuration

In this work we investigate the laminar flow of dilute and semidilute suspensions of neutrally buoyant spherical particles in straight ducts with square cross section. Two different sets of simulations are performed. Initially we study excluded-volume effects. To this aim we perform simulations in a Cartesian computational domain of size $L_x = 6h$, $L_z = 2h$, and $L_y = 2h$, where h is the duct half-width and x, y, and z are the streamwise and cross-stream directions (see Fig. 1).

The domain is discretized by a uniform ($\Delta x = \Delta z = \Delta y$) cubic mesh with $1296 \times 432 \times 432$ grid points for semidilute cases. In terms of particle radii, the computational domain has a size of $108a \times 36a \times 36a$, with a being the particle radius. A constant bulk velocity U_b is achieved by imposing a mean pressure gradient in the streamwise direction. Bulk and particle Reynolds number are here defined as $\mathrm{Re}_b = U_b 2h/\nu$ and $\mathrm{Re}_p = Re_b(a/h)^2$. We consider four different solid volume fractions: $\phi = 0.4\%$, 5%, 10%, and 20%. In this setup these correspond to 134, 1670, 3340, and 6680 particles, respectively. In all cases, particles are initially positioned randomly in the computational domain with zero linear and angular velocities. Each particle is discretized with $N_l = 1721$ Lagrangian control points while their radii are 12 Eulerian grid points long. Considering 12 grid points per particle radius ($\Delta x = 1/24$) is a good compromise in terms of computational cost and accuracy.

We also investigate the effects of bulk and particle Reynolds numbers and the duct to particle size ratio h/a for dilute suspensions with $\phi = 0.4\%$. We consider different combinations of Re_b and h/a resulting in different particle Reynolds numbers $\mathrm{Re}_p = \mathrm{Re}_b(a/h)^2$. The full set of simulations

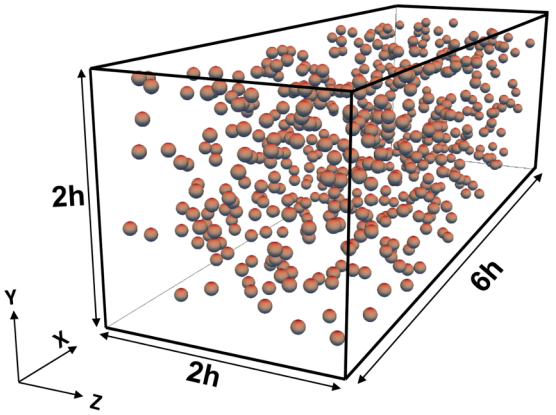

FIG. 1. Three-dimensional view of the duct geometry with few particles.

is summarized in Table I. Resolution is chosen to keep 12 grid points per particle radius for the different h/a ratios.

III. RESULTS

A. Validation

The code has been validated extensively against several test cases in previous studies [25,28,29]. In this study, first, we investigate how accurate it is to use the stress immersed boundary method to represent the duct walls. In particular, we compare our results on the mean flow to the analytic result reported by Shah and London [35]. The maximum discrepancy is found at the centerline and it is about 0.6% for the resolution used in this study.

We then perform a validation against the experimental results reported recently by Miura *et al.* [22] on the flow of dilute suspensions of neutrally buoyant spherical particles in a square duct. We perform a simulation to resemble the case presented in Fig. 5(a) of Ref. [22]. In particular, we consider a box of size $L_x = 144a$ and $L_y = L_z = 18a$, a bulk Reynolds number Re_b of 144, duct half-width to particle radius ratio $h/a = 9$, and volume fraction $\phi = 0.4\%$. After an initial transient, we compare the particle distribution across the duct to those found experimentally. Figure 2(a) shows

TABLE I. Summary of the simulations. The size of the computational domain is expressed in terms of particle radii and is denoted by L_x, L_y, L_z in the streamwise and wall-normal directions. The number of grid points in each direction N_x, N_y, N_z is chosen to keep 12 points per particle radius.

ϕ (%)	Re_b	Re_p	h/a	$L_x \times L_y \times L_z$	$N_x \times N_y \times N_z$
0.4	144	1.7	9	$144a \times 18a \times 18a$	$1728 \times 216 \times 216$
0.4	275	3.4	9	$72a \times 18a \times 18a$	$864 \times 216 \times 216$
0.4	550	6.8	9	$72a \times 18a \times 18a$	$864 \times 216 \times 216$
0.4	300	1.7	13	$78a \times 26a \times 26a$	$936 \times 312 \times 312$
0.4	550	3.2	13	$78a \times 26a \times 26a$	$936 \times 312 \times 312$
0.4	550	1.7	18	$108a \times 36a \times 36a$	$1296 \times 432 \times 432$
5	144	1.7	9	$72a \times 18a \times 18a$	$864 \times 216 \times 216$
5	550	6.8	9	$72a \times 18a \times 18a$	$864 \times 216 \times 216$
20	144	1.7	9	$72a \times 18a \times 18a$	$864 \times 216 \times 216$
5	550	1.7	18	$108a \times 36a \times 36a$	$1296 \times 432 \times 432$
10	550	1.7	18	$108a \times 36a \times 36a$	$1296 \times 432 \times 432$
20	550	1.7	18	$108a \times 36a \times 36a$	$1296 \times 432 \times 432$

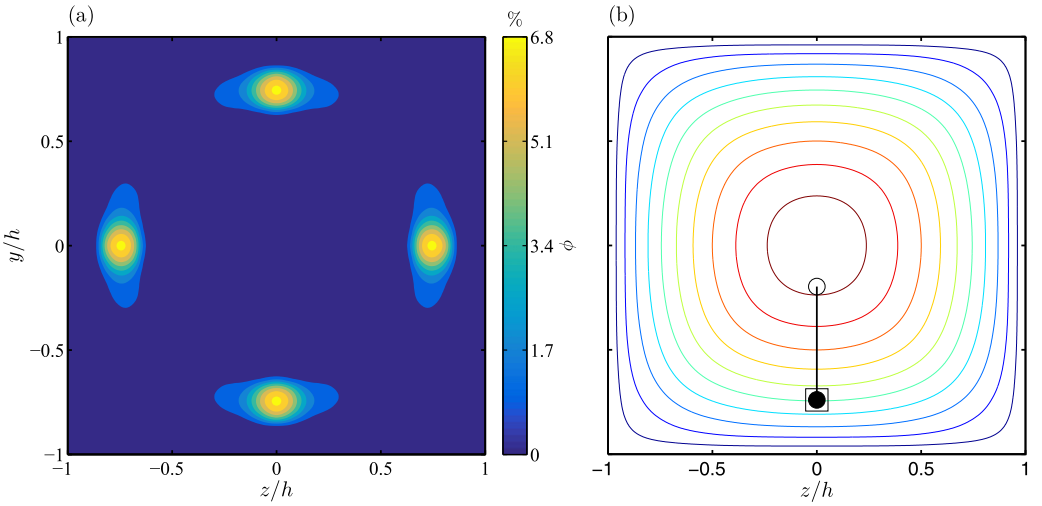

FIG. 2. (a) Spatial distribution of particles across the duct section for $\phi = 0.4\%$ and $\mathrm{Re}_b = 144$ ($\mathrm{Re}_p = 1.7$). (b) Equilibrium position of individual particle: ○, initial position; •, final position; □, Chun and Ladd's [17] final equilibrium position; and —, particle trajectory.

the particle concentration $\Phi(y,z)$ in the y-z plane (averaged in the streamwise direction and over time). Excellent agreement can be seen between our numerical results and the experimental data of Miura *et al.* [22] [see Fig. 5(a) of the cited paper].

The dependence of the particle's equilibrium position on the computational domain length is also checked. To this end, we perform a simulation in a shorter box, $L_x = 72a$, and the same Re_b and ϕ. The same final particle equilibrium position is found (not shown). Thus, we conclude that the results are independent of the box length for the values here considered.

In addition, we also examine the trajectory of an individual particle and compare it with the data previously reported by Chun and Ladd [17]. We assume $\mathrm{Re}_b = 100$ and $h/a = 9.1$ and compare our and their results in Fig. 2(b). The particle, initially slightly below the duct centerline, slowly migrates toward the same focusing position found by Chun and Ladd [17]. In particular, the focusing position is at the center of the duct wall ($z/h = 0$) at a distance of $0.74h$ from the centerline.

B. Semidilute suspensions

In this section we report and discuss the results obtained for different solid volume fractions ϕ at a constant bulk Reynolds number of $\mathrm{Re}_b = 550$ ($\mathrm{Re}_p = 1.7$) and duct to particle size ratio of $h/a = 18$. Note that all results shown hereinafter are obtained by taking averages over the eight symmetric triangles that form the duct cross section. We first show the particle concentration distribution $\Phi(y,z)$ across the duct cross section for $\phi = 0.4\%$, 5%, 10%, and 20% in Figs. 3(a)–3(d), respectively. The particle concentration distribution is defined as

$$\Phi(y,z) = \frac{1}{N_t N_x} \sum_{m=1}^{N_t} \sum_{i=1}^{N_x} \xi(x_{ijk}, t^m), \tag{7}$$

where N_t is the number of time steps considered for the average, t^m is the sampling time, and $\xi(x_{ijk}, t^m)$ is the particle indicator function at the location x_{ijk} and time t^m. The particle indicator function is equal to 1 for points x_{ijk} contained within the volume of a sphere and 0 in the fluid. At the lowest solid volume fraction $\phi = 0.4\%$, particles migrate preferentially toward two symmetric equilibrium positions near the duct corners [Fig. 3(a)]. However, some particles are also found uniformly distributed along the walls and in particular close to the wall centers at a distance of

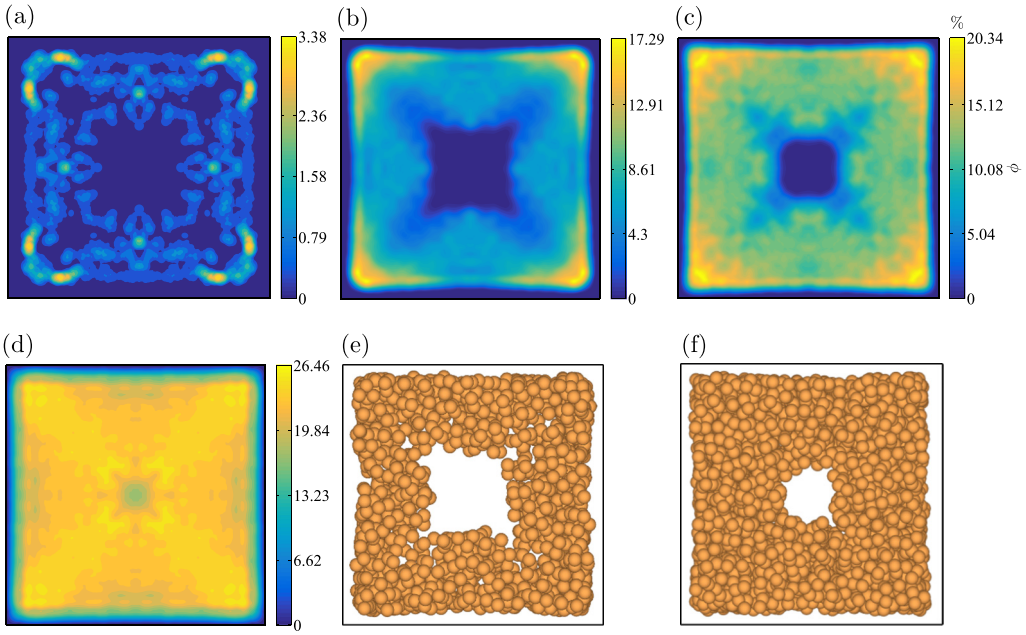

FIG. 3. Particle concentration distribution $\Phi(y,z)$ in the y-z plane (duct cross section) at $\mathrm{Re}_b = 550$ ($\mathrm{Re}_p = 1.7$) and $h/a = 18$ for (a) $\phi = 0.4\%$, (b) $\phi = 5\%$, (c) $\phi = 10\%$, (d) $\phi = 20\%$, and instantaneous snapshots of particle final positions in the y-z plane for (e) $\phi = 5\%$ and (f) $\phi = 10\%$.

approximately $0.6h$ away from the duct core. Figures 3(b) and 3(c) show that the particles tend to concentrate preferentially at the duct corners and less at the wall centers also for $\phi = 5\%$ and 10%. For these three volume fractions, the core of the duct is completely depleted of particles. In Figs. 3(e) and 3(f) we show instantaneous snapshots of particle positions in the duct cross section for $\phi = 5\%$ and 10%. At each instant, particles are always close to the duct walls. Hence, the particle concentration distribution $\Phi(y,z)$ at moderate ϕ appears to reflect the peculiar focusing positions obtained in dilute cases. However, at $\phi = 20\%$, particles distribute almost all over the cross section [see Fig. 3(d)]. One can still notice that the particle concentration is slightly larger at the corners and that stable layers of particles form close to the walls (as also found for channel flows [30]). Qualitatively similar results have been obtained for suspensions of neutrally buoyant spheres in pipe flows at solid volume fractions $\phi = 6\%$, 10%, and 20% [13]. It was shown that for $\phi = 6\%$ and 10% and $\mathrm{Re}_p \approx 0.35$, particles migrate from the core region toward the pipe wall. At $\phi = 20\%$, particles are uniformly distributed in the cross section with a maximum of the particle concentration at the pipe center and close to the wall. The maximum of local particle concentration at the pipe center for $\phi = 20\%$ is not present in our results for duct flow [see Fig. 3(d)]. The reason for this difference is probably the fact that the particle Reynolds number is larger ($\mathrm{Re}_p = 1.7$) than in the cited experiments ($\mathrm{Re}_p = 0.28$).

Despite different particle distributions across the duct cross section, residence times of particles at the duct wall center and duct corners are similar for $\phi = 5\%$ and 20%. We demonstrate this in Fig. 4 by calculating the cumulative probability density function $Q(\tau)$ of particles residence time τ in the corners or at the duct wall centers. We divide the computational domain into nine equal volumes of size $108a \times 12a \times 12a$: Four of these volumes contain the duct corners, four contain the duct wall centers, and the ninth contains the duct core (see the inset of Fig. 4). The residence time τ is defined as the maximum time a particle stays within the boundaries of one specific volume. The cumulative probability density function $Q(\tau)$ is calculated via the rank-order method [36], which is free from binning errors. The statistics are collected using the last 1200 nondimensional times. The

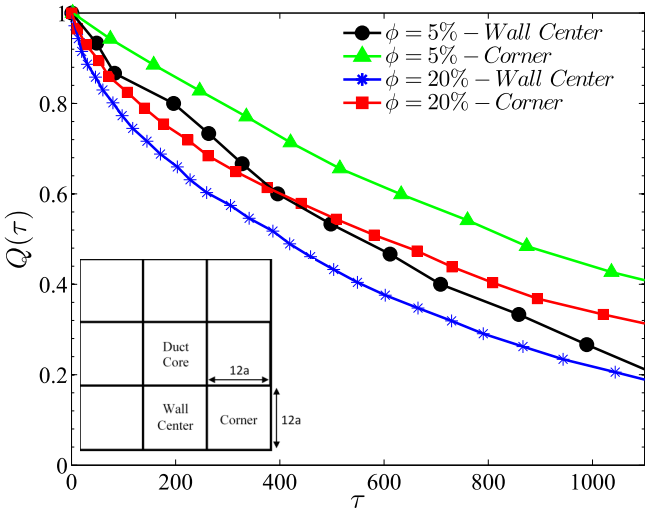

FIG. 4. Cumulative density function of residence times $Q(\tau)$ in the corners or at the wall centers for $\phi = 5$ and 20% at $\mathrm{Re}_b = 550$ ($\mathrm{Re}_p = 1.7$) and $h/a = 18$. The inset shows different regions of the duct for evaluation of the statistics.

results for $\phi = 5$ and 20% are shown in Fig. 4, where we see that $Q(\tau)$ is larger at the corners than at the wall centers (for the sake of clarity, the curves for $\phi = 10\%$ are not reported).

The streamwise mean particle velocity $U_p(y,z)$, normalized by the bulk velocity U_b, is illustrated in Figs. 5(a)–5(c) over the duct cross section for the different volume fractions ϕ. The contours resemble closely those of the streamwise fluid velocity except at the duct core, where it is fully depleted of particles for $\phi = 5\%$ and 10%. The uniform distribution of particles across the duct cross section for $\phi = 20\%$ results instead in a uniform streamwise mean velocity contour in the duct core [Fig. 5(c)].

The probability density functions (PDFs) of particle streamwise velocities U_p calculated at the duct corners and over the whole duct cross section are reported in Fig. 6. At the corners, we observe that the variance of the PDFs increases as the volume fraction increases [see Fig. 6(a)]. The mean value of the streamwise particle velocity is also found to increase with the volume fraction. As will be shown later, this behavior may be due to the fact that the streamwise mean fluid velocity at the duct corner increases with the solid volume fraction.

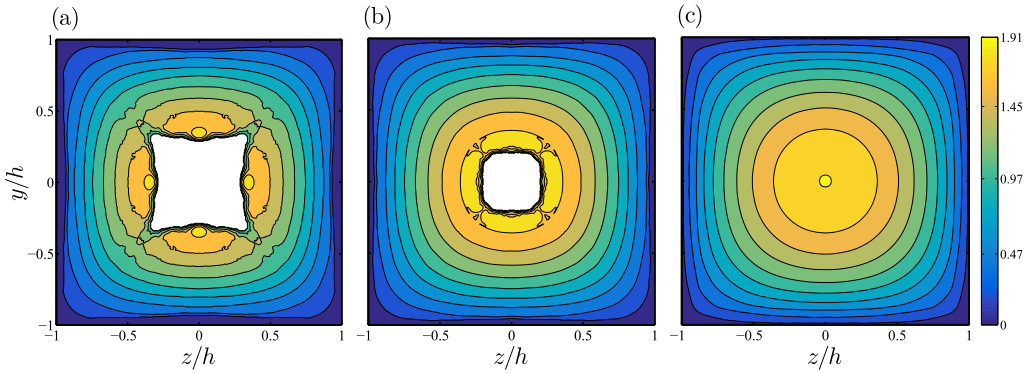

FIG. 5. Streamwise mean particle velocity contours U_p/U_b in the cross-stream y-z plane at $\mathrm{Re}_b = 550$ ($\mathrm{Re}_p = 1.7$) and $h/a = 18$ for (a) $\phi = 5\%$, (b) $\phi = 10\%$, and (c) $\phi = 20\%$.

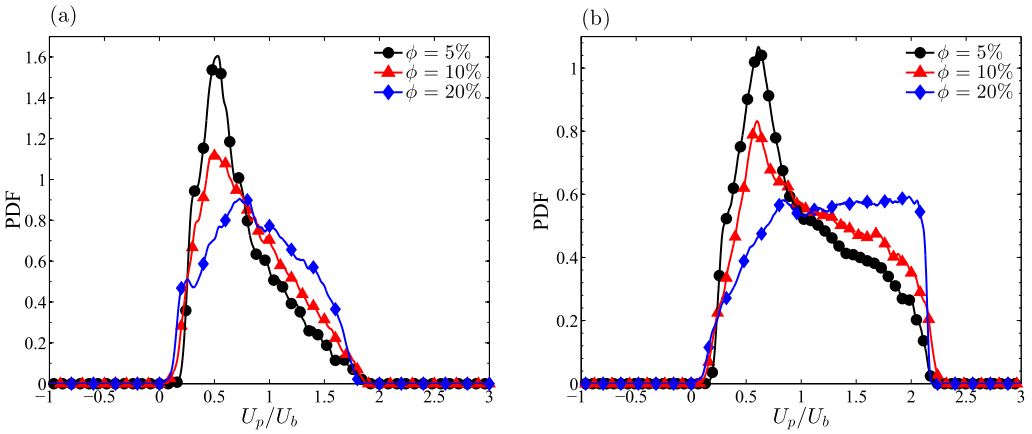

FIG. 6. Probability density function of particle velocities in the streamwise direction for different solid volume fractions at $\mathrm{Re}_b = 550$ ($\mathrm{Re}_p = 1.7$) and $h/a = 18$ (a) at the duct corner and (b) over the whole duct cross section.

The variance of the PDF of the particle streamwise velocity U_p in the whole duct is instead similar for all ϕ [see Fig. 6(b)]. However, as ϕ increases, particles are forced to distribute more uniformly across the duct and hence exhibit higher velocities toward the centerline. This leads to a progressive enhancement of the mean particle streamwise velocity and to a substantial change of the shape of the PDFs. Indeed, for $\phi = 20\%$ the mean streamwise particle velocity is 23% larger than that for $\phi = 5\%$; the different, more flattened, shape of the PDF is due to the uniform distribution of particles across the duct.

Figures 7(a)–7(c) show the streamwise velocity fluctuation contours $u'_{p,rms}(y,z)$ of the solid phase. We observe that the maxima of $u'_{p,rms}(y,z)$ are located close to the wall centers for all ϕ. At the highest ϕ, the maximum of $u'_{p,rms}(y,z)$ is almost twice that for $\phi = 5\%$. As expected, the fluctuations are lower at the duct corners where particles reside longer.

Fluid velocity fluctuations, absent in laminar regimes, are induced by the solid phase. Contours of the streamwise mean velocity fluctuations of the fluid phase $u'_{f,rms}$ are shown in Figs. 8(a)–8(c) for $\phi = 5\%$, 10%, and 20%. As for the particle velocity fluctuations, the maxima of $u'_{f,rms}$ are located in the proximity of the duct walls and increase by increasing the solid volume fraction. Spatially averaged streamwise fluid velocity fluctuations increase by 25% and 64% for $\phi = 10\%$ and 20%

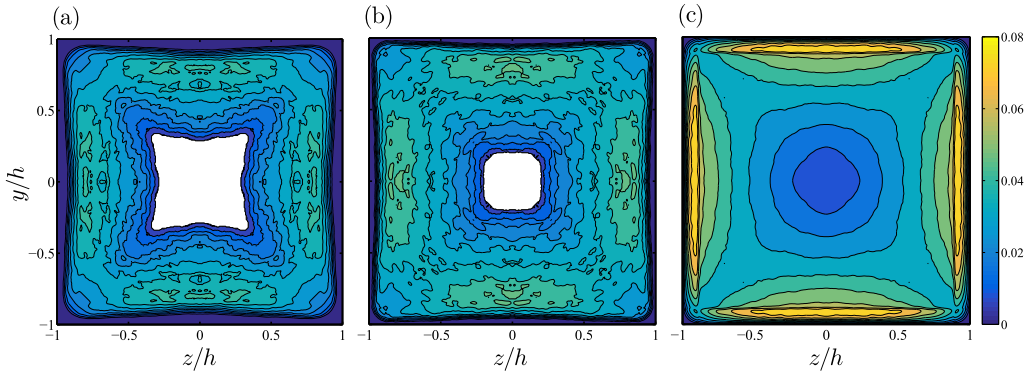

FIG. 7. Streamwise particle velocity fluctuation contours $u'_{p,rms}/U_b$ in the cross-stream y-z plane at $\mathrm{Re}_b = 550$ ($\mathrm{Re}_p = 1.7$) and $h/a = 18$ for (a) $\phi = 5\%$, (b) $\phi = 10\%$, and (c) $\phi = 20\%$.

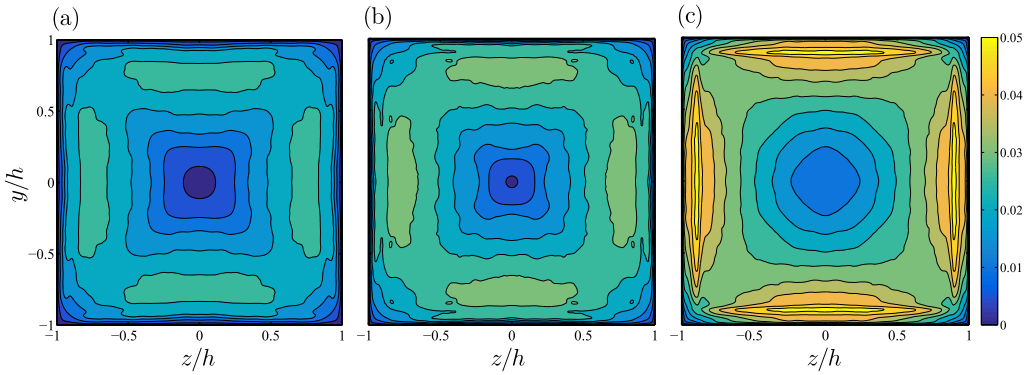

FIG. 8. Streamwise fluid velocity fluctuation contours $u'_{f,rms}/U_b$ in the cross-stream y-z plane at $\mathrm{Re}_b = 550$ ($\mathrm{Re}_p = 1.7$) and $h/a = 18$ for (a) $\phi = 5\%$, (b) $\phi = 10\%$, and (c) $\phi = 20\%$.

compared to the case $\phi = 5\%$. Comparing the data with the particle fluctuation velocities, it can be seen that $u'_{p,rms}/u'_{f,rms}$ is larger than 1 for all volume fractions under investigation.

Due to the solid phase, the mean fluid velocity profiles are altered with respect to the unladen case. In Fig. 9 we compare the streamwise mean fluid velocity profiles $U_f(y)$, normalized by the bulk velocity U_b, for each solid volume fraction ϕ at different spanwise locations z/h. One can see in Fig. 9(c) that at the wall bisector $z/h = 0$, the maximum velocity first increases for $\phi = 5\%$ and 10% and then decreases for $\phi = 20\%$. Blunted velocity profiles for pipe and channel flows of dense suspensions at low bulk Reynolds numbers have also been reported by other authors [37–40]. At $\phi = 5\%$ and 10%, particles migrate to the duct corners and depletion is seen at the duct center [Figs. 3(e) and 3(f)]. As the bulk velocity U_b is kept constant in our simulations, this results in a slight increase of the streamwise fluid velocity U_f around the centerline. On the other hand, at the highest volume fraction considered ($\phi = 20\%$) particles are homogeneously distributed across the duct cross section. Hence, the local viscosity of the suspension increases everywhere and this leads to the blunted velocity profile. Close to the duct corners $z/h = -0.8$, the maximum streamwise velocity is largest for $\phi = 20\%$ [see Fig. 9(a)]. Indeed, since U_b is constant, the reduction of the mean fluid velocity at the centerline for $\phi = 20\%$ leads to an expansion of the three-dimensional paraboloid describing the fluid velocity and hence to an increase of the fluid velocity at the corners.

The presence of particles in the flow increases the rate of energy dissipation and consequently the suspension viscosity and the wall shear stress. Figure 10(a) shows the distribution of the normalized shear stress $\tau_w/\overline{\tau_{w0}}$ along the duct wall, where $\overline{\tau_{w0}}$ denotes the mean value of wall shear stress pertaining the unladen flow. The results show a 16%, 36%, and 93% increase in the mean value of

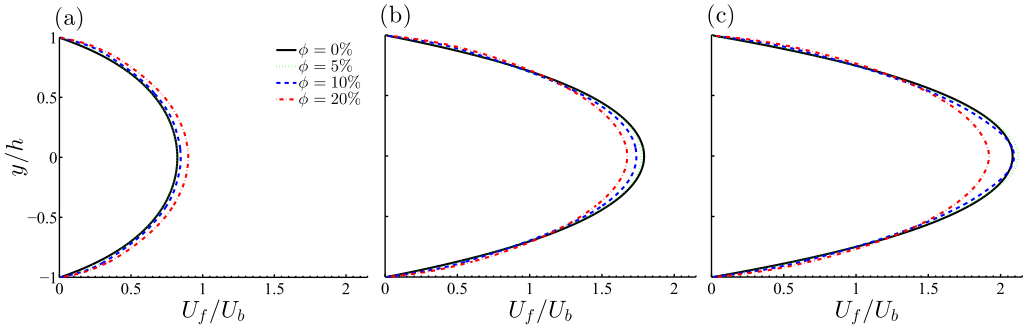

FIG. 9. Streamwise mean fluid velocity profiles U_f/U_b for different solid volume fractions at $\mathrm{Re}_b = 550$ ($\mathrm{Re}_p = 1.7$) and $h/a = 18$ at different spanwise locations along the y axis: (a) $z/h = -0.8$, (b) $z/h = -0.4$, and (c) $z/h = 0$.

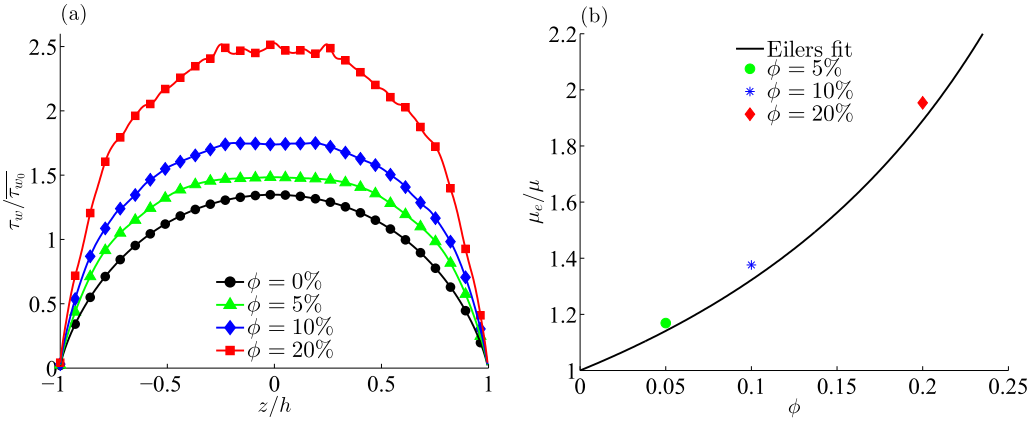

FIG. 10. (a) Distribution of shear stress along the duct wall and (b) relative viscosity of the suspensions under investigation in comparison with the Eilers fit: $\mu_r = \mu_e/\mu = [1 + 1.25\phi/(1 - \phi/0.6)]^2$. All cases presented here have the same bulk Reynolds number $\mathrm{Re}_b = 550$ ($\mathrm{Re}_p = 1.7$) and $h/a = 18$.

wall shear stress $\overline{\tau_w}$ for $\phi = 5\%$, 10%, and 20%, respectively, with respect to the unladen case. Taking the ratio between $\overline{\tau_w}$ and $\overline{\tau_{w0}}$, the relative viscosity $\mu_r = \mu_e/\mu$ (i.e., the ratio between the effective viscosity of the suspension and the viscosity of the fluid phase) can be determined. When plotted as a function of the solid volume fraction ϕ, we see that our results match empirical predictions given by the Eilers fit [2]. It should be noted that $\mathrm{Re}_p = \mathrm{Re}_b(a/h)^2 = 1.7$. Therefore, inertial effects are expected to be weak and this may explain the accuracy of the fit valid for vanishing inertia. Indeed, inertial shear thickening [41] is still weak in this case and we report just a weak underprediction of the effective viscosity.

C. Effect of geometry, bulk, and particle Reynolds numbers on the migration in dilute suspensions

In this section we discuss the influence of the bulk Reynolds number Re_b, duct to particle size ratio h/a, and particle Reynolds number Re_p on the spatial distribution of particles across the duct. To this aim, we focus on dilute suspensions of spheres with solid volume fraction $\phi = 0.4\%$. We consider three different duct to particle size ratios 9, 13, and 18. As the particle Reynolds number is a function of the bulk Reynolds number and the duct to particle size ratio, $\mathrm{Re}_p = Re_b(a/h)^2$, two parameters are steadily changed in three steps while one parameter is fixed. The results are shown in Figs. 11(a)–11(i), where we only report Reynolds numbers for laminar duct flow as turbulent diffusion would alter the particle distribution across the duct and no direct comparison could be made.

Figures 11(a)–11(c) show the particle concentration distribution $\Phi(y,z)$ at constant duct to particle size ratio $h/a = 9$ while increasing the bulk and consequently particle Reynolds numbers. As the bulk Reynolds number Re_b is increased from 144 to 275, particles that were initially focused at the wall centers [Fig. 11(a)] start to spread on a ring parallel to the duct walls with slightly larger concentration at the duct wall centers [see Fig. 11(b)]. A further increase in the bulk Reynolds number leads to the rupture of the ring. At $\mathrm{Re}_b = 550$, we observe the appearance of equilibrium positions at the duct corners and a low concentration focusing point close to the duct wall centers [see Fig. 11(c)]. These results are consistent with those by Nakagawa *et al.* [23], who studied the migration of single particles in square duct flows. For $\mathrm{Re}_b = 260$ and $h/a = 9$ these authors reported the existence of two equilibrium positions close to the duct corners in addition to a stable equilibrium position at the duct wall centers. One of the two equilibrium positions close to the duct corner is located on the diagonal, whereas the second appears between the diagonal and the wall center equilibrium position (see Fig. 6 of Ref. [23]). A similar pattern can be seen in Fig. 11(b) of the present study

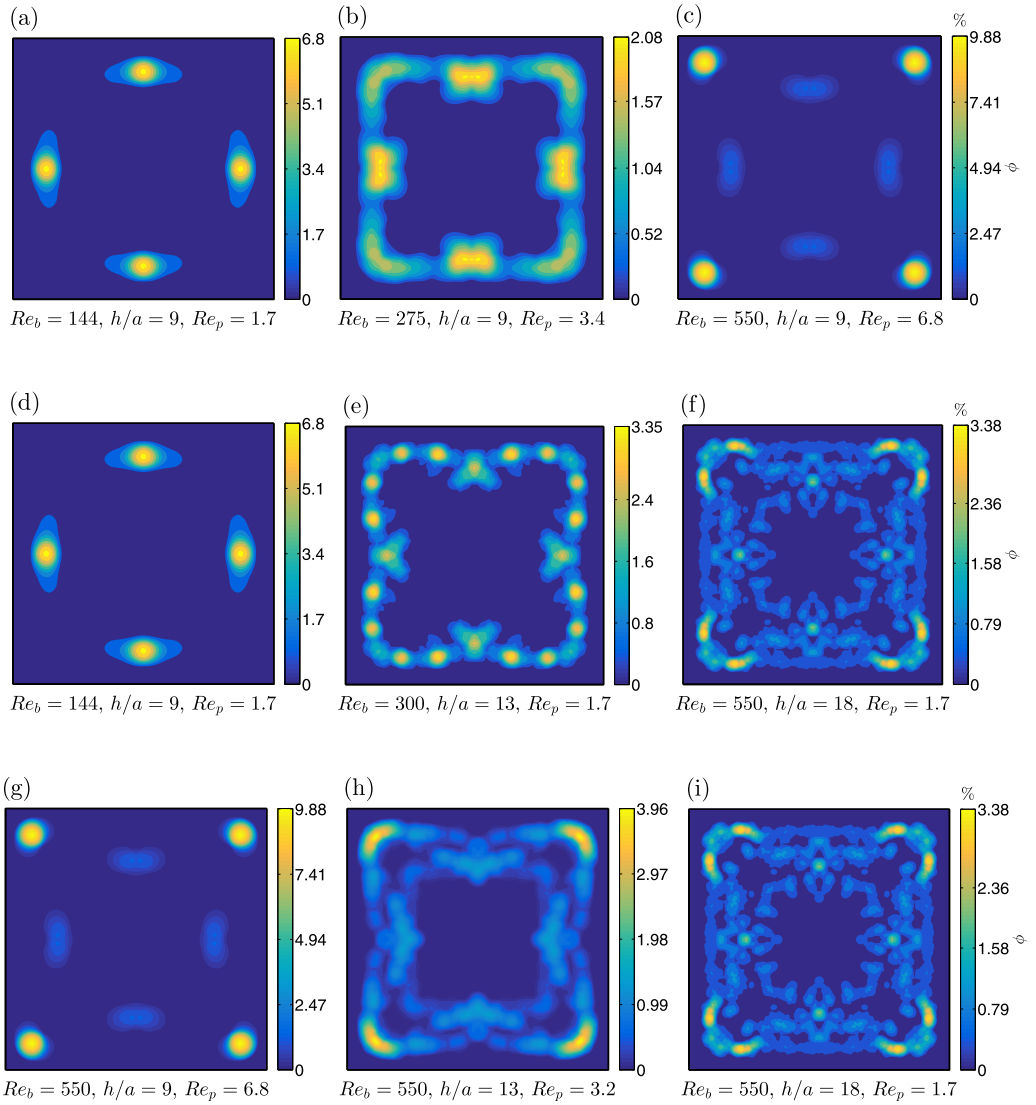

FIG. 11. Particle concentration distribution $\Phi(y,z)$ in the duct cross section for $\phi = 0.4\%$: (a)–(c) constant particle relative size, $h/a = 9$, and increasing bulk and particle Reynolds numbers Re_b and Re_p; (d)–(f) constant $\mathrm{Re}_p = 1.7$ for increasing Re_b and h/a; and (g)–(i) constant $\mathrm{Re}_b = 550$ for Re_p and h/a.

for $\phi = 0.4\%$, $h/a = 9$, and $\mathrm{Re}_b = 275$, where two symmetric equilibrium positions emerge close to the duct corners. In addition, Nakagawa *et al.* [23] showed that by increasing the bulk Reynolds number from 260 to 514, the equilibrium position at the wall center moves toward the duct core. The same behavior is observed in our simulations for $\mathrm{Re}_b = 550$ where the equilibrium position at the duct wall center is closer to the duct center in comparison to the case with $\mathrm{Re}_b = 275$. In fact, the location of the maximum local particle concentration changes from about $0.7h$ for $\mathrm{Re}_b = 275$ to approximately $0.6h$ for $\mathrm{Re}_b = 550$. Similar results were found experimentally by Miura *et al.* [22]. Interestingly, these results are in contrast to what has been observed in pipe flow where the particle equilibrium position has been shown to approach the wall as the bulk Reynolds number Re_b is increased (see the work of Segre and Silberberg [7] and Matas *et al.* [10]).

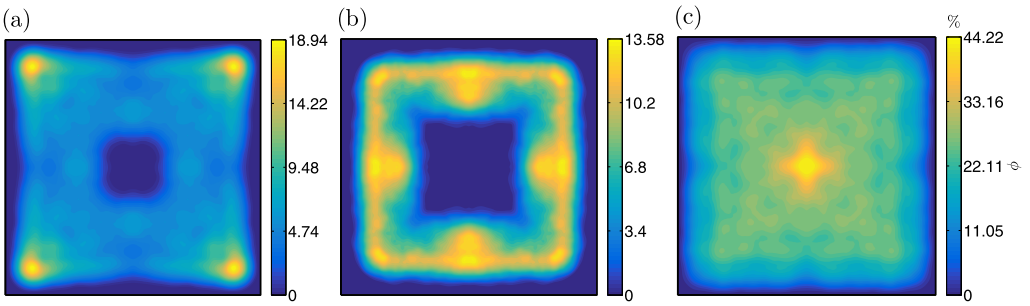

FIG. 12. Particle concentration distribution $\Phi(y,z)$ in the duct cross section for semidilute suspensions at constant relative size $h/a = 9$ and different bulk and particle Reynolds numbers: (a) $\mathrm{Re}_b = 550$, $\phi = 5\%$, and $\mathrm{Re}_p = 6.8$; (b) $\mathrm{Re}_b = 144$, $\phi = 5\%$, and $\mathrm{Re}_p = 1.7$; and (c) $\mathrm{Re}_b = 144$, $\phi = 20\%$, and $\mathrm{Re}_p = 1.7$.

Figures 11(d)–11(f) illustrate the particle spatial distribution across the duct cross section when the particle Reynolds number is kept constant at $\mathrm{Re}_p = 1.7$ while adjusting the bulk Reynolds number Re_b and duct to particle size ratio h/a. Qualitatively, we observe a particle distribution similar to that shown in Figs. 11(a)–11(c) for constant h/a. For $\mathrm{Re}_b = 300$ and $h/a = 13$ as shown in Fig. 11(e), we observe multiple equilibrium positions on the heteroclinic orbits that connect the wall center and corner equilibrium positions. The existence of additional equilibrium positions on the heteroclinic orbits for $\mathrm{Re}_b \geqslant 260$ had also been hypothesized by Nakagawa *et al.* [23].

Comparing Figs. 11(c) and 11(f), we note that particles distribute more uniformly across the cross section for larger h/a and the same bulk Reynolds number of $\mathrm{Re}_b = 550$. Moreover, the regions of higher concentration are located at two symmetric points around each corner. Therefore, for larger h/a these symmetric equilibrium positions appear at higher bulk Reynolds numbers as particles experience less inertia (i.e., smaller Re_p) in comparison to the case with $h/a = 9$.

Finally, to further explore the role of the bulk Reynolds number Re_b, we show in Figs. 11(g)–11(i) the particle concentration $\Phi(y,z)$ at constant bulk Reynolds number $\mathrm{Re}_b = 550$ for different particle Reynolds numbers Re_p and duct to particle size ratios h/a. The results show similar patterns at the same bulk Reynolds number Re_b: All cases in Figs. 11(g)–11(i) display clear equilibrium positions at the corners and weaker focusing at the wall center. This shows that changes in the bulk Reynolds numbers lead to the most significant variations of the particle distribution. Therefore, the bulk Reynolds number appears to be the dominant parameter in the system. However, increasing the duct to particle size ratio, the particle concentration at the duct corner broadens until two separate equilibrium positions appear for $h/a = 18$ [Fig. 11(i)]. By increasing the duct to particle size ratio h/a at the same bulk Reynolds number Re_b, particles experience weaker velocity gradients (i.e., inertial effects), resulting in a more uniform distribution across the duct cross section.

In Sec. III B we observed similar particle distribution pattern for dilute ($\phi = 0.4\%$) and semidilute ($\phi = 5\%$) suspensions at $\mathrm{Re}_b = 550$ and $h/a = 18$ [Figs. 3(a) and 3(b)]. In addition, Fig. 12(a) shows the particle distribution for $\phi = 5\%$, $\mathrm{Re}_b = 550$, and $h/a = 9$. These results, together with the case presented in Fig. 3(c) for $\phi = 0.4\%$, $\mathrm{Re}_b = 550$, and $h/a = 9$, show that at the same bulk Reynolds number $\mathrm{Re}_b = 550$, particles are preferentially concentrated at the duct corners rather than at the wall centers regardless of the different duct to particle size ratio h/a and solid volume fraction ϕ. Hence, we would expect a similar behavior for $\phi = 0.4\%$ and $\phi = 5\%$ also at the bulk Reynolds number of $\mathrm{Re}_b = 144$. To test this conjecture, we have performed a simulation with volume fraction $\phi = 5\%$, $h/a = 9$, and $\mathrm{Re}_b = 144$. The resulting particle distribution at steady state is shown in Fig. 12(b). It can be seen that in addition to the wall center equilibrium position [where $\Phi(y,z)$ is the maximum], particles also accumulate around the corners at this low bulk Reynolds number of $\mathrm{Re}_b = 144$. It should be mentioned that the corner equilibrium position is absent at the same bulk Reynolds number of $\mathrm{Re}_b = 144$ and low solid volume fraction $\phi = 0.4\%$ [Fig. 11(a)]. Therefore, while particles still undergo inertial migration away from the core, the exact particle distribution

depends also on the volume fraction ϕ. At the highest volume fraction $\phi = 20\%$ and low bulk Reynolds number $\mathrm{Re}_b = 144$ [see Fig. 12(c)] the inertial focusing appears to be almost lost and particles concentrate mostly at the duct center region. Elsewhere in the cross section the particle concentration is substantially uniform. From these results, we can conclude that for suspensions of neutrally buoyant particles at moderately high concentration ($\phi \geqslant 5\%$) and low bulk Reynolds numbers Re_b, the exact particle distribution depends on both the nominal solid volume fraction ϕ and the bulk Reynolds number Re_b. These observations can have implications for inertial microfluidics at high throughput.

To summarize, the results in this section indicate that the key parameter in defining particle migration and focusing positions at low ϕ is the bulk Reynolds number Re_b. Similar particle distributions across the duct are obtained for equal and finite bulk Reynolds numbers (greater than 100) and different h/a. The small differences in the distributions are due to the duct to particle size ratio h/a (and hence to particle inertia). In particular, our systematic study shows that at lower Re_b, particles focus at the wall centers. Increasing the bulk Reynolds number, particles first form a ringlike structure close to the four walls and finally accumulate mostly at the duct corners (higher Re_b).

At a constant Re_b, however, larger particles experience stronger velocity gradients than smaller particles. The particle Reynolds number is hence different for larger and smaller particles and this results in a slight modification of the exact particle distribution across the duct. Indeed, for $\mathrm{Re}_b = 550$ and $h/a = 9$ we see that almost all particles are precisely at the corners while fewer focus closer to the wall centers. For $h/a = 18$, the results are similar. However, particles do not accumulate precisely at the corners (i.e., on the diagonal) and the distribution is slightly more uniform close to the walls than for the previous case. For semidilute suspensions ($\phi = 5\%$–20%), while the inertial effect is dominant at the highest bulk Reynolds number $\mathrm{Re}_b = 550$, the excluded-volume effects have a significant role in determining the final particle distribution at the lowest bulk Reynolds number $\mathrm{Re}_b = 144$ investigated here.

D. Secondary flows

No secondary motions are present in a laminar duct flow. Typically secondary flows appear at high bulk Reynolds numbers once the flow becomes turbulent. According to Prandtl [42], there are two kinds of secondary flows: skew induced and Reynolds stress induced. The former are absent in fully developed turbulent duct flows while the latter are produced by the deviatoric Reynolds shear stress $\langle v_f' w_f' \rangle$ and the cross-stream Reynolds stress difference $\langle v_f'^2 \rangle - \langle w_f'^2 \rangle$ (where $\langle \cdot \rangle$ denotes averaged quantities). When a solid phase is dispersed in the liquid, particle-induced stresses generate cross-stream secondary motions also in originally laminar flows.

The results of the present study show the existence of secondary flows induced by particles in dilute suspensions. In Figs. 13(a)–13(f) we report the crossflow velocity magnitude $\sqrt{V_f^2 + W_f^2}$ and vector fields for different cases with $\phi = 0.4\%$. We clearly see that the intensity of these secondary flows is stronger close to the particle focusing positions. For $h/a = 9$ and $\mathrm{Re}_b = 144$ particles focus at the wall centers [cf. Fig. 11(a)] and, accordingly, secondary motions are stronger around the focusing positions and point from the core toward the wall centers [Fig. 13(a)]. As documented in Sec. III B, when the bulk Reynolds number Re_b is increased, these four focusing positions are lost and particles form a ringlike structure close to the walls [Fig. 11(b)]. The corresponding secondary motions are displayed in Fig. 13(b): Their intensity reduces significantly due to the more uniform particle distributions across the duct cross section. Further increasing the bulk Reynolds number $\mathrm{Re}_b = 550$, particles focus at the duct corners [Fig. 11(c)]. Consequently, the secondary motion is more evident at these locations, now directed toward the corners along the bisectors [Fig. 13(c)]. Comparing Figs. 13(a) and 13(c), we note that the cross-stream motions are directed from the duct core to the locations of particle focusing.

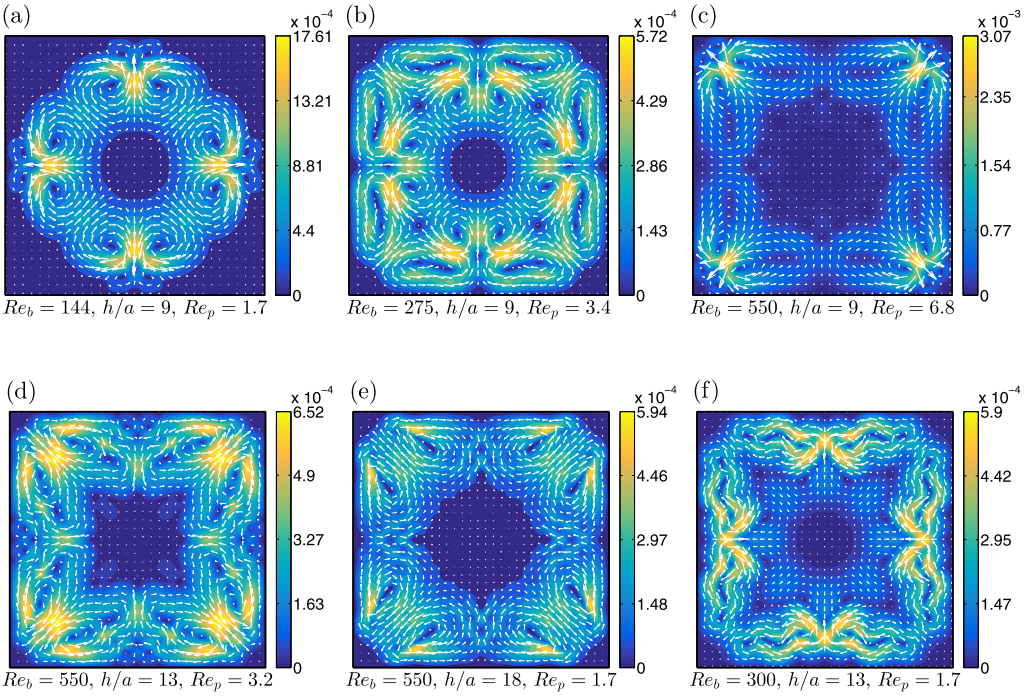

FIG. 13. Contour plot of crossflow velocity magnitude $\sqrt{V_f^2 + W_f^2}$ and vector field for $\phi = 0.4\%$ and Reynolds numbers and particle size reported in the legend. For comparison, (a)–(c) correspond to the cases presented in Figs. 11(a)–11(c), (d) and (e) correspond to the cases in Figs. 11(h) and 11(i), and (f) corresponds to the case in Fig. 11(e).

Further, we observe in Fig. 11(c) that for $h/a = 9$ and $\mathrm{Re}_b = 550$, the local particle concentration at the duct corners is higher than that found at the wall centers for $\mathrm{Re}_b = 144$ [Fig. 11(a)]. Moreover, Fig. 13(c) shows that the secondary flow intensity increases for $\mathrm{Re}_b = 550$ with respect to the cases at $\mathrm{Re}_b = 144$ and 275 [Figs. 13(a) and 13(b)]. These observations suggest that the intensity of the secondary flows is determined by the local particle concentration. However, the intensity of these secondary flows is small and less than 0.4% of U_b.

Figures 13(d) and 13(e) show the crossflow velocity magnitude $\sqrt{V_f^2 + W_f^2}$ and vector fields for two cases with the same bulk Reynolds number $\mathrm{Re}_b = 550$ and different duct to particle size ratios h/a of 13 and 18. We see that both the maximum value of the local particle concentration [Fig. 11(i)] and the secondary flow intensity are higher for the duct with $h/a = 13$. At smaller h/a and constant Re_b, when the particle inertia (i.e., the particle Reynolds number Re_p) and particle-induced stresses are higher, stronger secondary flows are generated. Finally, we report the secondary flow pattern for bulk Reynolds number $\mathrm{Re}_b = 300$ and $h/a = 13$ in Fig. 11(f). This configuration has the same particle Reynolds number ($\mathrm{Re}_p = 1.7$) and similar maximum value of local particle concentration as the case with $\mathrm{Re}_b = 550$ and $h/a = 18$ [see Figs. 11(e) and 11(i)]. In agreement with the previous results, we observe similar secondary flow intensity in Figs. 13(e) and 13(f).

Next we explore the dependence of the fluid secondary motions on the solid volume fraction ϕ. To this aim, contours of the crossflow velocity magnitude $\sqrt{V_f^2 + W_f^2}$ and velocity vectors are reported in Figs. 14(a)–14(c) for the semidilute cases ($\phi = 5\%$–20%) in the wider duct with $h/a = 18$ and bulk Reynolds number of $\mathrm{Re}_b = 550$. The maximum intensity of these secondary flows is still low, about 0.2% of the bulk velocity U_b (approximately 1/10 of that found in turbulent duct flows). The maximum of the secondary cross-stream velocity is similar for $\phi = 5\%$ and 10%, while it

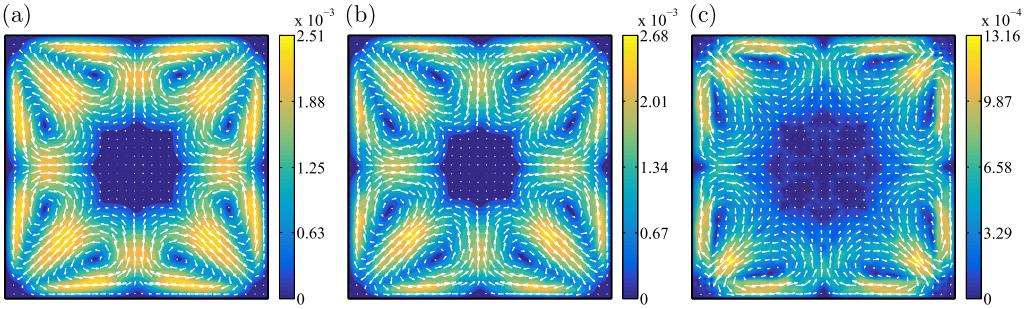

FIG. 14. Contour plots of the crossflow velocity magnitude $\sqrt{V_f^2 + W_f^2}$ and velocity vectors for $\mathrm{Re}_b = 550$, $\mathrm{Re}_p = 1.7$, $h/a = 18$, and (a) $\phi = 5\%$, (b) $\phi = 10\%$, and (c) $\phi = 20\%$.

substantially decreases for $\phi = 20\%$. The mean of the crossflow velocity magnitude $\sqrt{V_f^2 + W_f^2}$ initially increases and then decreases as the volume fraction ϕ increases as shown in Fig. 15, where we report the mean values of $\sqrt{V_f^2 + W_f^2}$ for each ϕ. All results are normalized by the mean value obtained for $\phi = 0.4\%$. It is also interesting to note that, in semidilute suspensions, when particles accumulate at the corners, the secondary flow patterns are similar to those found in turbulent flows. Particle-induced stresses act in a similar fashion to Reynolds stresses and consequently lead to similar secondary flows. These secondary flows, although weak, convect the mean velocity from regions of large shear along the walls toward regions of low shear. This convection occurs along the corner bisectors, resulting in a lower mean streamwise velocity at the walls (and particularly at the wall centers) [43]. This effect can also be seen in the contours of mean particle streamwise velocity U_p (which closely resemble the contours of the mean fluid streamwise velocity) (see Fig. 5). This behavior is attenuated as the solid volume fraction increases and the secondary flows are progressively damped.

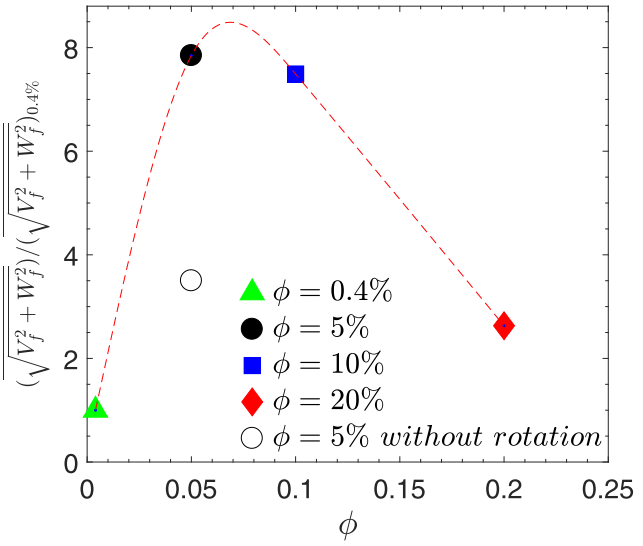

FIG. 15. Mean value of $\sqrt{V_f^2 + W_f^2}$ normalized by the mean value of $(\sqrt{V_f^2 + W_f^2})_{0.4\%}$ for semidilute suspensions with $\phi = 5\%$, 10%, and 20%. Also shown is the result from a simulation with $\phi = 5\%$, in which particles are constrained not to rotate. The dashed line is for visualization.

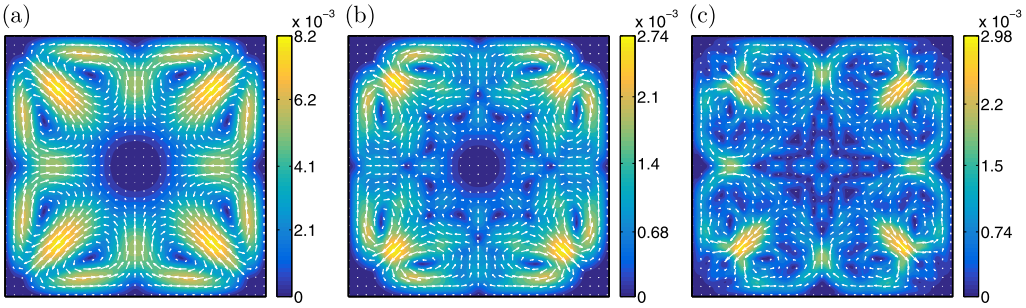

FIG. 16. Contour plots of the crossflow velocity magnitude $\sqrt{V_f^2 + W_f^2}$ and velocity vectors for semidilute suspensions at constant relative size $h/a = 9$ and different bulk and particle Reynolds numbers: (a) $\mathrm{Re}_b = 550$, $\phi = 5\%$, and $\mathrm{Re}_p = 6.8$; (b) $\mathrm{Re}_b = 144$, $\phi = 5\%$, and $\mathrm{Re}_p = 1.7$; and (c) $\mathrm{Re}_b = 144$, $\phi = 20\%$, and $\mathrm{Re}_p = 1.7$.

Figures 16(a)–16(c) show the crossflow motions for the semidilute cases ($\phi = 5\%$ and 20%) presented in Sec. III C at constant $h/a = 9$ and different bulk Reynolds numbers Re_b [see Figs. 12(a)–12(c)]. Comparing Figs. 16 and 14(a), it can be clearly seen that the secondary motion is stronger for bigger particles, i.e., $h/a = 9$, at the same volume fraction $\phi = 5\%$ and bulk Reynolds number $\mathrm{Re}_b = 550$. Figure 16(b) shows the presence of crossflow motion for $\phi = 5\%$ at lower bulk Reynolds number $\mathrm{Re}_b = 144$. A significant reduction in the secondary flow intensity can be seen as the bulk Reynolds number Re_b decreases from 550 to 144 at the same h/a. These results are in agreement with our previous observation about the role of particle inertia and the local particle concentration on the intensity of the secondary motion in dilute suspensions. Finally, Fig. 16(c) shows the secondary motion pattern for $\phi = 20\%$ at $\mathrm{Re}_b = 144$ and $h/a = 9$. Interestingly, while particles accumulate mostly at the duct center [Fig. 12(c)], the counterrotating vortices point toward the duct corners along the bisector and their intensity is higher than for $\phi = 5\%$ [see Fig. 16(b)]. This result is in contrast to what is observed for $h/a = 18$ and $\mathrm{Re}_b = 550$, where the secondary flow intensity decreases for $\phi = 20\%$. Hence, the threshold ϕ above which the maximum secondary flow intensity decreases changes with both Re_b and h/a. However, it must be noted that for $\phi = 20\%$ the mean value of the secondary flow intensity in the cross section is smaller than for $\phi = 5\%$, as also found for $\mathrm{Re}_b = 550$ and $h/a = 18$ (not shown here).

To gain further insight into the role of particle angular velocities on the intensity of secondary flows, we performed an additional simulation at $\mathrm{Re}_b = 550$, $h/a = 18$, and $\phi = 5\%$ in which we artificially impose zero particle rotation (i.e., constant null angular velocities) while allowing translations. The mean value of the crossflow velocity magnitude reduces significantly ($\sim$55%) with respect to the reference case at $\phi = 5\%$ (see Fig. 15). This confirms that the intensity of secondary motions strongly depends on the particle angular velocities.

At finite particle Reynolds number Re_p, when inertia plays an important role, the flow field around a particle is altered and the fore-aft symmetry of the streamlines is lost [44]. Amini *et al.* [45] investigated the flow field around a translating and rotating spherical particle in Poiseuille flow at finite particle Reynolds number. These authors showed the existence of a pair of recirculating zones perpendicular to the primary flow in the vicinity of the particle. Here we investigate the flow field around an individual particle moving through a duct at its equilibrium position at $\mathrm{Re}_b = 100$ and $h/a = 10$. We first consider a particle free to move and rotate and then artificially set the spanwise particle angular velocity to zero, $\omega_z = 0$, to quantify the effect of particle rotation on the intensity of the recirculating flows (calculated as in Ref. [45]). As shown in Fig. 17, the intensity of the flow around the particle is directly related to the particle angular velocity and drastically decreases by setting $\omega_z = 0$. Moreover, the particle focusing position changes in the absence of rotation and moves slightly toward the duct core. The presence of this local secondary flow near the particle is also reported by Shao *et al.* [46] at bulk Reynolds number $\mathrm{Re}_b = 1000$ in pipe flow.

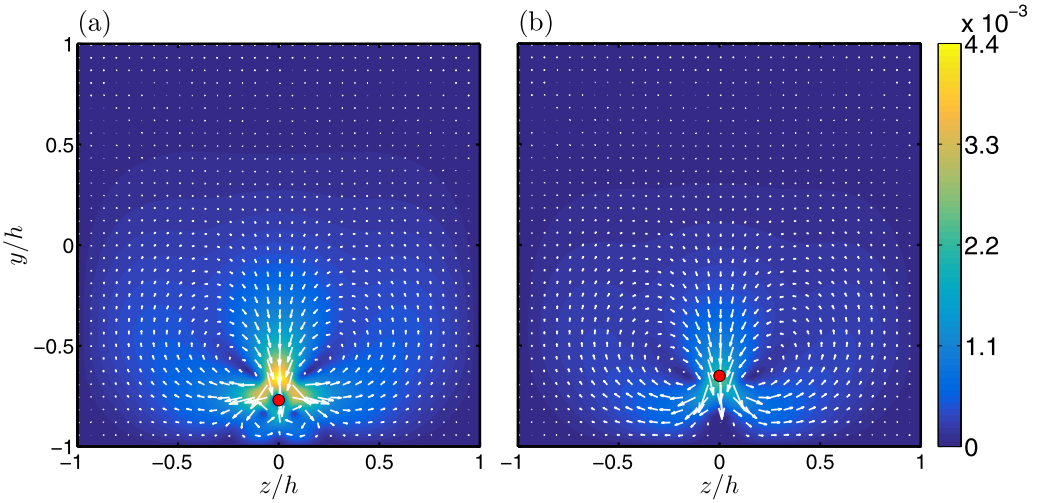

FIG. 17. Contour plot of the crossflow velocity magnitude $\sqrt{V_f^2 + W_f^2}$ and velocity vectors around a particle: (a) the particle moves and rotates freely through the duct and (b) the particle moves downstream with spanwise angular velocity set to zero. The red circle shows the position of the particle center.

IV. CONCLUSION

We presented results from direct numerical simulations of laminar duct flow of suspensions of finite-size neutrally buoyant spherical particles at different solid volume fractions. We used an immersed boundary method for the fluid-solid interactions with lubrication and collision models for the short-range particle-particle (particle-wall) interactions. The stress immersed boundary method was applied to generate the duct walls. Initially we investigated excluded-volume effects in dilute and semidilute suspensions with $\phi = 0.4\%$, 5%, 10%, and 20%, for duct to particle size ratio $h/a = 18$ and bulk Reynolds number $\mathrm{Re}_b = 550$. We showed that for solid volume fractions $\phi = 5\%$ and 10%, particles mostly accumulate at the duct corners and particle depletion can be seen at the core of the duct. For $\phi = 20\%$, particles distribute uniformly over the whole domain with slightly higher concentration at the diagonal of the the duct. For all ϕ, particles reside longer at the corners than at the wall centers. An effective viscosity increase leads to a blunted streamwise fluid velocity profile at the duct center at a solid volume fraction $\phi = 20\%$. Nonetheless, the Eilers fit was able to predict the increase of dissipation in the duct as inertial effects (at the particle scale) are small, $\mathrm{Re}_p = 1.7$.

We then investigated the interactions and role of Re_b, Re_p, and h/a on the behavior of dilute suspensions with $\phi = 0.4\%$. Initially, we kept the duct to particle size ratio constant at $h/a = 9$ and increased the bulk and particle Reynolds numbers. For $\mathrm{Re}_b = 144$ particles focused at the walls centers. Increasing Re_b, particles initially formed a ring close to the walls and finally, for $\mathrm{Re}_b = 550$, accumulated preferentially at the duct corners and partially closer to the wall centers, at a distance of $0.6h$ away from the core. The particle equilibrium position at the wall center moved toward the duct core when Re_b was increased from 144 to 550. The same behavior of the evolution of the particle local volume fraction was observed at constant particle Reynolds number $\mathrm{Re}_p = 1.7$ when increasing the bulk Reynolds number Re_b and duct to particle size ratio h/a. Finally, for constant bulk Reynolds number $\mathrm{Re}_b = 550$ and different particle Reynolds numbers Re_p and duct to particle size ratios h/a, we found a high concentration around the duct corners and less at the wall centers. The same behavior was observed for $\phi = 5\%$, $h/a = 9$, and the same bulk Reynolds number $\mathrm{Re}_b = 550$. In the same manner, for lower bulk Reynolds number $\mathrm{Re}_b = 144$, $h/a = 9$, and $\phi = 5\%$, we would have expected particles to accumulate at the walls centers (since for $\phi = 0.4\%$ the focusing positions are located there). Instead, we observed accumulation of particles around the corners in addition to the particle equilibrium position at the wall centers. We also showed that at high solid volume

fraction $\phi = 20\%$, $h/a = 9$, and $\mathrm{Re}_b = 144$, particle concentrate mostly at the duct core region and no inertial migration of particles was observed. Therefore, for the range of h/a and Re_b investigated here, we concluded that in dilute suspensions the particle focusing position is mainly governed by the bulk Reynolds number. In addition, excluded-volume effects seem to be another key parameter in determining the particle concentration distribution in semidilute suspensions ($\phi = 5\%$–20%) at low bulk Reynolds number. Thus, trivially extending results for single particles to semidilute suspensions may lead to wrong predictions.

Secondary flows are generated in the duct due to the presence of particles. At low volume fractions $\phi = 0.4\%$, secondary flows appear around the particle focusing positions and the corresponding vorticity strength is dominated by the local particle concentration. We showed that for $\mathrm{Re}_b = 550$ and $h/a = 18$, the mean secondary flow intensity initially increases with the solid volume fraction from $\phi = 0.4\%$ to $\phi = 5\%$, while it decreases for $\phi > 5\%$. In the semidilute regime ($\phi \geqslant 5\%$), the secondary flows appear as a pair of counterrotating vortices directed toward the corners, along the bisectors. Since they resemble closely the secondary flows found in turbulent duct flows, particle-induced stresses generate secondary flows in a similar fashion to Reynolds stresses. Their intensity is however $1/10$ of that found in turbulent duct flows. We saw that the mean intensity of these secondary flows decreases above $\phi = 5\%$. Indeed, when many particles are injected in the duct, the cross-stream motions generated by a particle are quickly disrupted by its neighbors.

Finally, we studied the relation between particle rotation and secondary flows. We constrained a single particle to translate without rotation and we observed that the intensity of the secondary vortices substantially decreases. We also noticed that the focusing position (initially at the wall center) moves vertically closer to the duct core. We also inhibited particle rotation in the semidilute suspension with $\phi = 5\%$, $\mathrm{Re}_b = 550$, and $h/a = 18$ and found that the mean intensity of the secondary flows is reduced by 55%. Therefore, these secondary flows strongly depend on particle rotation.

In the future, it will be interesting to study turbulent duct flows laden with finite-size spheres and observe the modification of secondary flows, particle statistics, and turbulence modulation.

ACKNOWLEDGMENTS

This work was supported by the European Research Council Grant No. ERC-2013-CoG-616186, TRITOS, from the Swedish Research Council (VR), through the Outstanding Young Researcher Award. The authors gratefully acknowledge the COST Action MP1305, "Flowing matter" and computer time provided by Swedish National Infrastructure for Computing (SNIC).

APPENDIX: TEMPORAL EVOLUTION OF THE PARTICLE CONCENTRATION

In this Appendix we briefly discuss the effect of Re_b, Re_p, and ϕ on the temporal evolution of the cases under the investigation. In Table II we report the dimensionless time T^* needed for the simulations to reach their final steady state in terms of particle concentration distribution $\Phi(y,z)$. We define this as the time needed by the local particle concentration around the focusing points to reach the final mean value. Here time is nondimensionalized by viscous units $[(2a)^2/\nu]$.

For constant $h/a = 9$ and $\phi = 0.4\%$, the results show that the particles reach the equilibrium positions faster by increasing the bulk Reynolds number Re_b from 144 to 550. For constant bulk Reynolds number $\mathrm{Re}_b = 550$ and increasing h/a, we notice that it takes longer for the particles to evolve and reach their equilibrium positions. Indeed, this is due to the fact that particle inertia, i.e., Re_p, is less significant at higher h/a. Overall, we see that for the dilute suspensions $\phi = 0.4\%$, the particle evolution time T^* is reduced by increasing the particle Reynolds number Re_p.

Finally, for semidilute cases, we show that T^* decreases by increasing the solid volume fraction ϕ from 5% to 20%. At higher concentrations there is progressively less space available for particle migrations and the final average particle distribution is reached faster.

TABLE II. Time to reach the final steady-state particle distribution for the different cases considered.

ϕ (%)	Re_b	Re_p	h/a	T^*
0.4	144	1.7	9	56
0.4	275	3.4	9	45
0.4	550	6.8	9	34
0.4	300	1.7	13	64
0.4	550	3.2	13	43
0.4	550	1.7	18	79
5	144	1.7	9	100
20	144	1.7	9	44
5	550	6.8	9	51
5	550	1.7	18	110
10	550	1.7	18	80
20	550	1.7	18	49

[1] D. Di Carlo, Inertial microfluidics, Lab Chip **9**, 3038 (2009).

[2] J. J. Stickel and R. L. Powell, Fluid mechanics and rheology of dense suspensions, Annu. Rev. Fluid Mech. **37**, 129 (2005).

[3] J. F. Morris, A review of microstructure in concentrated suspensions and its implications for rheology and bulk flow, Rheol. Acta **48**, 909 (2009).

[4] W. Fornari, L. Brandt, P. Chaudhuri, C. U. Lopez, D. Mitra, and F. Picano, Rheology of Confined Non-Brownian Suspensions, Phys. Rev. Lett. **116**, 018301 (2016).

[5] V. Doyeux, S. Priem, L. Jibuti, A. Farutin, M. Ismail, and P. Peyla, Effective viscosity of two-dimensional suspensions: Confinement effects, Phys. Rev. Fluids **1**, 043301 (2016).

[6] E. Guazzelli and J. F. Morris, *A Physical Introduction to Suspension Dynamics* (Cambridge University Press, Cambridge, 2011), Vol. 45.

[7] G. Segre and A. Silberberg, Behaviour of macroscopic rigid spheres in Poiseuille flow part 2. Experimental results and interpretation, J. Fluid Mech. **14**, 136 (1962).

[8] L. Zeng, S. Balachandar, and P. Fischer, Wall-induced forces on a rigid sphere at finite Reynolds number, J. Fluid Mech. **536**, 1 (2005).

[9] J. P. Matas, J. F. Morris, and E. Guazzelli, Lateral forces on a sphere, Oil Gas Sci. Technol. **59**, 59 (2004).

[10] J.-P. Matas, J. F. Morris, and É. Guazzelli, Inertial migration of rigid spherical particles in poiseuille flow, J. Fluid Mech. **515**, 171 (2004).

[11] J.-P. Matas, J. F. Morris, and É. Guazzelli, Lateral force on a rigid sphere in large-inertia laminar pipe flow, J. Fluid Mech. **621**, 59 (2009).

[12] Y. Morita, T. Itano, and M. Sugihara-Seki, Equilibrium radial positions of neutrally buoyant spherical particles over the circular cross-section in poiseuille flow, J. Fluid Mech. **813**, 750 (2017).

[13] M. Han, C. Kim, M. Kim, and S. Lee, Particle migration in tube flow of suspensions, J. Rheol. **43**, 1157 (1999).

[14] D. R. Gossett, W. M. Weaver, A. J. Mach, S. C. Hur, H. T. K. Tse, W. Lee, H. Amini, and D. Di Carlo, Label-free cell separation and sorting in microfluidic systems, Anal. Bioanal. Chem. **397**, 3249 (2010).

[15] A. Karimi, S. Yazdi, and A. M. Ardekani, Hydrodynamic mechanisms of cell and particle trapping in microfluidics, Biomicrofluidics **7**, 021501 (2013).

[16] H. Amini, W. Lee, and D. Di Carlo, Inertial microfluidic physics, Lab Chip **14**, 2739 (2014).

[17] B. Chun and A. J. C. Ladd, Inertial migration of neutrally buoyant particles in a square duct: An investigation of multiple equilibrium positions, Phys. Fluids **18**, 031704 (2006).

[18] D. Di Carlo, J. F. Edd, K. J. Humphry, H. A. Stone, and M. Toner, Particle Segregation and Dynamics in Confined Flows, Phys. Rev. Lett. **102**, 094503 (2009).
[19] K. Hood, S. Lee, and M. Roper, Inertial migration of a rigid sphere in three-dimensional Poiseuille flow, J. Fluid Mech. **765**, 452 (2015).
[20] Y.-S. Choi, K.-W. Seo, and S.-J. Lee, Lateral and cross-lateral focusing of spherical particles in a square microchannel, Lab Chip **11**, 460 (2011).
[21] M. Abbas, P. Magaud, Y. Gao, and S. Geoffroy, Migration of finite sized particles in a laminar square channel flow from low to high Reynolds numbers, Phys. Fluids **26**, 123301 (2014).
[22] K. Miura, T. Itano, and M. Sugihara-Seki, Inertial migration of neutrally buoyant spheres in a pressure-driven flow through square channels, J. Fluid Mech. **749**, 320 (2014).
[23] N. Nakagawa, T. Yabu, R. Otomo, A. Kase, M. Makino, T. Itano, and M. Sugihara-Seki, Inertial migration of a spherical particle in laminar square channel flows from low to high Reynolds numbers, J. Fluid Mech. **779**, 776 (2015).
[24] I. Lashgari, M. N. Ardekani, I. Banerjee, A. Russom, and L. Brandt, Inertial migration of spherical and oblate particles in straight ducts, J. Fluid Mech. **819**, 540 (2017).
[25] W.-P. Breugem, A second-order accurate immersed boundary method for fully resolved simulations of particle-laden flows, J. Comput. Phys. **231**, 4469 (2012).
[26] H. Brenner, The slow motion of a sphere through a viscous fluid towards a plane surface, Chem. Eng. Sci. **16**, 242 (1961).
[27] P. Costa, B. J. Boersma, J. Westerweel, and W.-P. Breugem, Collision model for fully resolved simulations of flows laden with finite-size particles, Phys. Rev. E **92**, 053012 (2015).
[28] Francesco Picano, Wim-Paul Breugem, and Luca Brandt, Turbulent channel flow of dense suspensions of neutrally buoyant spheres, J. Fluid Mech. **764**, 463 (2015).
[29] W. Fornari, F. Picano, and L. Brandt, Sedimentation of finite-size spheres in quiescent and turbulent environments, J. Fluid Mech. **788**, 640 (2016).
[30] I. Lashgari, F. Picano, W. P. Breugem, and L. Brandt, Channel flow of rigid sphere suspensions: Particle dynamics in the inertial regime, Int. J. Multiphase Flow **78**, 12 (2016).
[31] W. Fornari, A. Formenti, F. Picano, and L. Brandt, The effect of particle density in turbulent channel flow laden with finite size particles in semi-dilute conditions, Phys. Fluids **28**, 033301 (2016).
[32] W.-P. Breugem, V. Van Dijk, and R. Delfos, Flows through real porous media: X-ray computed tomography, experiments, and numerical simulations, J. Fluids Eng. **136**, 040902 (2014).
[33] W. P. Breugem and B. J. Boersma, Direct numerical simulations of turbulent flow over a permeable wall using a direct and a continuum approach, Phys. Fluids **17**, 025103 (2005).
[34] M. B. J. M. Pourquie, W. P. Breugem, and B. J. Boersma, Some issues related to the use of immersed boundary methods to represent square obstacles, Int. J. Multiscale Comput. Eng. **7**, 509 (2009).
[35] R. K. Shah and A. L. London, *Laminar Flow Forced Convection in Ducts: A Source Book for Compact Heat Exchanger Analytical Data* (Academic, New York, 2014).
[36] D. Mitra, J. Bec, R. Pandit, and U. Frisch, Is Multiscaling an Artifact in the Stochastically Forced Burgers Equation? Phys. Rev. Lett. **94**, 194501 (2005).
[37] A. Karnis, H. L. Goldsmith, and S. G. Mason, The kinetics of flowing dispersions: I. Concentrated suspensions of rigid particles, J. Colloid Interface Sci. **22**, 531 (1966).
[38] R. E. Hampton, A. A. Mammoli, A. L. Graham, N. Tetlow, and S. A. Altobelli, Migration of particles undergoing pressure-driven flow in a circular conduit, J. Rheol. **41**, 621 (1997).
[39] C. J. Koh, P. Hookham, and L. G. Leal, An experimental investigation of concentrated suspension flows in a rectangular channel, J. Fluid Mech. **266**, 1 (1994).
[40] M. K. Lyon and L. G. Leal, An experimental study of the motion of concentrated suspensions in two-dimensional channel flow. Part 1. Monodisperse systems, J. Fluid Mech. **363**, 25 (1998).
[41] F. Picano, W.-P. Breugem, D. Mitra, and L. Brandt, Shear Thickening in Non-Brownian Suspensions: An Excluded Volume Effect, Phys. Rev. Lett. **111**, 098302 (2013).
[42] L. Prandtl, Über die ausgebildete turbulenz, Verh. 2nd Intl. Kong. Tech. Mech. Zürich [NACA Report No. 435, 1926 (unpublished), p. 62].
[43] L. Prandtl, *The Essentials of Fluid Dynamics* (Blackie, London, 1952).

[44] G. Subramanian and D. L. Koch, Inertial effects on the transfer of heat or mass from neutrally buoyant spheres in a steady linear velocity field, Phys. Fluids **18**, 073302 (2006).

[45] H. Amini, E. Sollier, W. M. Weaver, and D. Di Carlo, Intrinsic particle-induced lateral transport in microchannels, Proc. Natl. Acad. Sci. USA **109**, 11593 (2012).

[46] X. Shao, Z. Yu, and B. Sun, Inertial migration of spherical particles in circular Poiseuille flow at moderately high Reynolds numbers, Phys. Fluids **20**, 103307 (2008).